Adaptation of temperature optima of vegetation productivity across global biomes

Mengtian Huang[1], Shilong Piao[1,2,3*], Philippe Ciais[4], Josep Peñuelas[5,6], Xuhui Wang[1], Trevor F. Keenan[7,8], Shushi Peng[1], Joseph A. Berry[9], Kai Wang[1], Jiafu Mao[10], Ramdane Alkama[11], Alessandro Cescatti[11], Matthias Cuntz[12], Hannes De Deurwaerder[13], Mengdi Gao[1], Yue He[1], Yongwen Liu[1], Yiqi Luo[14], Ranga B. Myneni[15], Shuli Niu[16], Xiaoying Shi[10], Wenping Yuan[17], Hans Verbeeck[13], Tao Wang[2,3], Jin Wu[18], Ivan A. Janssens[19]

[1] Sino-French Institute for Earth System Science, College of Urban and Environmental Sciences, Peking University, Beijing 100871, China.

[2] Key Laboratory of Alpine Ecology and Biodiversity, Institute of Tibetan Plateau Research, Chinese Academy of Sciences, Beijing 100085, China.

[3] Center for Excellence in Tibetan Earth Science, Chinese Academy of Sciences, Beijing 100085, China.

[4] Laboratoire des Sciences du Climat et de l'Environnement, CEA CNRS UVSQ, Gif-sur-Yvette 91191, France.

[5] CREAF, Cerdanyola del Vallès, Barcelona 08193, Catalonia, Spain.

[6] CSIC, Global Ecology Unit CREAF-CSIC-UAB, Bellaterra, Barcelona 08193, Catalonia, Spain.

[7] Lawrence Berkeley National Laboratory, Berkeley, California 94720, USA.

[8] Department of Environmental Science, Policy and Management, UC Berkeley, Berkeley, California 94720, USA.

[9] Department of Global Ecology, Carnegie Institution for Science, Stanford, California 94305, USA.

[10] Climate Change Science Institute and Environmental Sciences Division, Oak Ridge National Laboratory, Oak Ridge, TN, USA.

[11] European Commission, Joint Research Centre, Institute for Environment and Sustainability, Ispra, Italy.

[12] Department Computational Hydrosystems, UFZ Helmholtz Centre for Environmental Research, Permoserstraße 15, 04318 Leipzig, Germany.

[13] CAVElab Computational & Applied Vegetation Ecology, Facultyof Bioscience Engineering, Ghent University, Coupure Links 653, B-9000 Gent, Belgium.

[14] Department of Biological Sciences, Northern Arizona University, Arizona, 86011, USA.

[15] Department of Earth and Environment, Boston University, Boston, Massachusetts 02215, USA.

[16] Key Laboratory of Ecosystem Network Observation and Modeling, Institute of Geographic Sciences and Natural Resources Research, Chinese Academy of Sciences, Beijing, China.

[17] School of Atmospheric Sciences, Center for Monsoon and Environment Research, Sun Yatsen University, Guangzhou 510275, China.

[18] Environmental & Climate Sciences Department, Brookhaven National Laboratory, Upton, NY, 11973, USA.

[19] Centre of Excellence PLECO (Plant and Vegetation Ecology), Department of Biology, University of Antwerp, Universiteitsplein 1, B-2610 Wilrijk, Belgium.

* Correspondence to: slpiao@pku.edu.cn

The global distribution of the optimum air temperature of ecosystem-level gross primary productivity (T_{opt}^{eco}) is poorly understood, despite its importance for ecosystem carbon uptake under future warming. We provide empirical evidence for the existence of such an optimum, using measurements of in situ eddy covariance and satellite-derived proxies, and report its global distribution. T_{opt}^{eco} is consistently lower than the physiological optimum temperature of leaf-level photosynthesis, which typically exceeds 30 °C. The global average T_{opt}^{eco} is estimated to be 23±6 ºC, with warmer regions having higher T_{opt}^{eco} values than colder regions. In tropical forests, particularly, T_{opt}^{eco} is close to growing-season air temperature and is projected to fall below it under all scenarios of future climate, suggesting a limited safe operating space for these ecosystems under future warming.

Understanding how photosynthesis responds to warming has been a focus in plant research in recent decades, and most of the existing knowledge comes from leaf-scale measurements[1-4]. Most leaf-scale temperature response curves show that photosynthesis increases with temperature up to an optimum temperature (T_{opt}^{leaf}), which typically occurs in the 30-40°C temperature range[5,6]. Above this optimum temperature, foliar photosynthesis sharply declines as electron-transport and Rubisco enzymatic capacities become impaired[7]. Field et al. [8] first suggested that ecosystem-scale optimum temperature (T_{opt}^{eco}) may differ from T_{opt}^{leaf}. At ecosystem scale, elevated air temperatures do limit canopy photosynthesis by other processes than leaf carboxylation rates. For instance, elevated air temperatures reduce hydraulic conductivities in the soil-root-stem-canopy continuum (hydraulics; e.g. ref 6), accelerate leaf ageing and increase leaf thickness (phenology; e.g. ref 9), and control stomatal closure, because a higher temperature usually comes with a higher vapor pressure deficit (VPD)[10].

Empirical leaf-scale photosynthesis-temperature relationships[11] have been directly incorporated into global ecosystem models, with variants to account for acclimation, i.e. a temporal adjustment of optimum photosynthetic temperature to air temperature during growth[5,12,13]. This direct scaling of temperature responses from leaves to ecosystems partly determines model projections of Gross Primary Productivity (GPP) and CO_2 uptake by terrestrial ecosystems in climatic scenarios. Verifying the existence of T_{opt}^{eco} in real world ecosystems, defining its spatial distribution across and within biomes and understanding the relationships between T_{opt}^{eco}, prevailing air temperature and T_{opt}^{leaf} are important for evaluating models and understanding the impacts of various targets of climatic warming targets on ecosystem productivity.

In this study, we formulate and test the following hypotheses: (i) T_{opt}^{eco} is higher for biomes where air temperature during growth is warmer (adaptation), (ii) T_{opt}^{eco} is lower than T_{opt}^{leaf} for any given ecosystem, because the above mentioned limitations of plant hydraulics and phenology emerge before temperature begins to impair foliar photosynthesis, and (iii) tropical forests already operate near a high T_{opt}^{eco} above which canopy photosynthesis may decrease with even moderate air temperature warming[14,15]. Here we defined T_{opt}^{eco} as the daytime air temperature at which GPP is highest over a period of several years, thus T_{opt}^{eco} can be empirically determined from productivity observations and proxies (see Methods).

Results and discussion

We first applied this approach on time series of daily GPP derived from CO_2 flux measurements at 153 globally distributed eddy covariance sites and found that a robust estimate of T_{opt}^{eco} could

be derived at 125 out of 153 sites (see Methods). T_{opt}^{eco} values derived from the FLUXNET data range from 8.2°C to 35.8°C (Fig. 1a, Supplementary Table 1). Tropical sites have higher T_{opt}^{eco} values than temperate and boreal sites (Supplementary Fig. 1), implying a dependence of T_{opt}^{eco} on background climate. The FLUXNET multi-site analysis further indicates that across sites T_{opt}^{eco} values are positively correlated with growing-season mean daily maximum air temperature ($T_{max\ gs}^{air}$, see calculation in Methods) (R=0.46, P<0.01), with a spatial linear regression slope of 0.61 °C per °C across sites (Fig. 1a). Overall, these results confirm our first hypothesis stating that higher T_{opt}^{eco} values occur where higher growth temperatures prevail, in support of findings of Baldocchi et al.[16].

Since eddy covariance measurements do not have a continuous spatial coverage, we also used satellite observations known to be highly correlated with photosynthetic activity[17], that is, GPP proxies. The first proxy used is the near-infrared reflectance of terrestrial vegetation (NIR_V, the product of total-scene NIR reflectance (NIR_T) by the Normalized Difference Vegetation Index (NDVI). NIR_V was proven to have a high temporal correlation with GPP at flux tower sites[17]. Satellite observations of NIR_T and NDVI from the Terra Moderate Resolution Imaging Spectroradiometer (MODIS) were used to calculate NIR_V for the period of 2001-2013 (see Methods). NIR_V-derived T_{opt}^{eco} is comparable with that estimated from eddy covariance flux tower measurements (Fig. 1b), which gives support to using the NIR_V proxy for a global mapping of T_{opt}^{eco}. The average T_{opt}^{eco} over the global vegetated areas is estimated to be 23±6 °C (mean ± 1 SD) with large spatial gradients in latitude. As shown in Fig. 1c, maximum values close to 30°C mainly appear over tropical forests, savannas and drylands and minimum values near 10°C prevail at high-latitudes and in mountainous regions (Fig. 1c). This spatial pattern of T_{opt}^{eco} is

116 robust to the choice of a particular climate forcing dataset, or to the method used to estimate T_{opt}^{eco}
117 (Supplementary Fig. 2, see also Methods). Similar results are also found for other GPP proxies
118 (vegetation greenness (NDVI)[18], Enhanced Vegetation Index (EVI)[19], sun-induced vegetation
119 fluorescence (Sun-induced Chlorophyll Fluorescence, SIF)[20]), or when daily mean air
120 temperature (T_{mean}^{air}) is used instead of daily maximum air temperature (T_{max}^{air}) to calculate T_{opt}^{eco}
121 (Supplementary Figs. 3-6, see also Methods). Note that although the covariance between air
122 temperature, atmospheric VPD and solar radiation may confuse the direct effect of air
123 temperature on vegetation productivity, we verified that neither VPD nor radiation is the
124 dominant factor determining the pattern of T_{opt}^{eco} at the global scale (see Methods).
125
126 In order to test the second hypothesis, we compared satellite-derived T_{opt}^{eco} with T_{opt}^{leaf} from the
127 responses of maximum Rubisco-limited carboxylation rates (V_{cmax}) to temperature from leaf-
128 scale measurements for 36 species[5]. We found that T_{opt}^{eco} is indeed lower than T_{opt}^{leaf}
129 (Supplementary Fig. 7), with a larger difference between T_{opt}^{leaf} and T_{opt}^{eco} for needle-leaved than
130 for broad-leaved forests. This difference may originate from the fact that T_{opt}^{eco} is additionally
131 limited by high VPD during hot and dry periods[6] and by soil-moisture deficits during extensive
132 dry episodes[21], under real world conditions. In contrast, leaf-level photosynthesis measurements
133 to determine V_{cmax} are never performed on drought-affected leaves. Moreover, tree hydraulic
134 conductance is limited, and may not be able to keep up with the increasing evaporative demands
135 at higher temperatures, especially for needle-leaved species that have a lower stem-water
136 conductivity[22]. Based on NIR_V-derived results, we did diagnose a lower T_{opt}^{eco} for needle-leaved
137 than for broad-leaf forests under the same growth temperature conditions (Supplementary Table
138 2). In addition, plant phenology controls leaf age, vitality (photosynthetic rates) and foliar density

(e.g. Leaf Area Index, LAI)[23], and may therefore co-determine ecosystem-level temperature limitations and the optimum temperature for canopy photosynthesis[24]. It is also important to remark when comparing T_{opt}^{leaf} with T_{opt}^{eco} that leaf-scale measurements are often limited to sunlit leaves, which could lead to a positive bias of existing in-situ T_{opt}^{leaf} measurements. What's more, the tree species database used by Kattge & Knorr[5] from which T_{opt}^{leaf} data were collected does not include any tropical species. This may explain why global models prescribed with T_{opt}^{leaf} give very uncertain results for tropical biomes.

The relationship between T_{opt}^{eco} and background climate is shown in Fig. 1d. The sampling of leaf-scale studies does not provide consistent evidence about the dependence of T_{opt}^{leaf} on climate, with positive correlations between T_{opt}^{leaf} and growing season air temperature in a set of studies[1, 5, 25-27] attributed to evolutionary adaptation[7], but no clear relationship between T_{opt}^{leaf} and growing season temperature in the review from Sage & Kubien[7]. In contrast, T_{opt}^{eco} inferred from satellite GPP proxies in our study increases with $T_{max\,gs}^{air}$ across the globe. In temperature-precipitation space, the spatial sensitivity of T_{opt}^{eco} to $T_{max\,gs}^{air}$ (the slope of the linear regression between these two variables) is lower than 1 for any precipitation bin (Fig. 1d), suggesting that spatial gradients of T_{opt}^{eco} are smaller than those of $T_{max\,gs}^{air}$, possibly because hydraulic and phenological limitations further limit T_{opt}^{eco} across spatial gradients. In fact, the spatial sensitivity of T_{opt}^{eco} to $T_{max\,gs}^{air}$ generally increases with increasing mean annual precipitation (Fig. 1d), even though T_{opt}^{eco} is not significantly correlated with precipitation after controlling for the effect of $T_{max\,gs}^{air}$ (Fig. 1d). This thermal adaptation of T_{opt}^{eco}, suggested by the positive spatial slope of the T_{opt}^{eco}-air temperature relation, is also observed across biomes. As shown in Fig. 2, there is a significant

positive correlation between T_{opt}^{eco} and $T_{max\,gs}^{air}$ with a slope of 0.76 across different biomes. Among biomes, the largest mean T_{opt}^{eco} is found in tropical evergreen broad-leaved forest (29±3 °C), and the smallest mean T_{opt}^{eco} (13±3 °C) in cold grasslands covering the Tibetan Plateau (Fig. 2 and Supplementary Fig. 8).

Both model results and very limited observational studies suggest a decrease in canopy photosynthesis of tropical forests at high temperature[15, 28-31] which led us to formulate the third hypothesis of tropical forests already operating at T_{opt}^{eco} being close to $T_{max\,gs}^{air}$ implying that canopy photosynthesis may decrease in case of future warming[14, 15]. This hypothesis is verified from the data shown in Fig. 3 (see also Supplementary Fig. 9). T_{opt}^{eco} is indeed only slightly (1.4 °C) lower than $T_{max\,gs}^{air}$ over tropical evergreen forests, suggesting a small 'safety margin' for photosynthesis under future warming. In contrast, arctic (north of 65^{o}N) and boreal (50^{o}N-65^{o}N) ecosystems exhibit substantially larger safety margins, i.e. a larger positive difference between T_{opt}^{eco} and $T_{max\,gs}^{air}$ (Fig. 3a and Supplementary Fig. 9). Analysis of the 16-day averaged T_{max}^{air} distribution during the period when T_{opt}^{eco} is observed further shows that the rank of T_{opt}^{eco} in the T_{max}^{air} distribution is already near the highest quantile of T_{max}^{air} (>70%) for tropical evergreen forests (Supplementary Fig. 10). Based on this result, one may expect that rising air temperature in the future may limit or decrease vegetation productivity in tropical forests, but not in temperate or boreal ecosystems.

Global terrestrial daily maximum air temperature is projected to rise by 1.9 °C under the RCP2.6 low warming climate scenario and by 5.6 °C under the RCP8.5 scenario by 2100[32]. We compared these $T_{max\,gs}^{air}$ projections with the present-day distribution of T_{opt}^{eco} with a focus on tropical

evergreen forests, where optimum temperature is currently just below the limit of $T_{max\,gs}^{air}$ (see Methods; Fig. 3b and 3c). The key uncertainty in this discussion is, however, whether or not T_{opt}^{eco} will acclimate and follow the increase in $T_{max\,gs}^{air}$. We therefore looked at possible acclimation from time series of T_{opt}^{eco} retrieved from the Advanced Very High Resolution Radiometer (AVHRR) NDVI, which spans the last 30 years and comprises almost a 1°C temperature range. NDVI-derived T_{opt}^{eco} did not have a significant trend over the last three decades (Supplementary Fig. 11), suggesting that either the recent 1°C warming is not large enough to elicit an acclimation response from ecosystems, given decadal variability[33], or that acclimation does not occur at multi-decadal timescales. Also the annual T_{opt}^{eco} derived from FLUXNET estimates of GPP did not exhibit a positive trend and was not significantly correlated with annual variations of $T_{max\,gs}^{air}$, although the FLUXNET time series are probably too short to properly evaluate trends of T_{opt}^{eco} related to possible acclimation processes (Supplementary Fig. 12). Because we detected no indication for its existence, we first assumed no acclimation in the comparison of future $T_{max\,gs}^{air}$ projections from climate models with the current distribution of T_{opt}^{eco}. Under this assumption, the average $T_{max\,gs}^{air}$ of tropical evergreen forests will exceed the current value of T_{opt}^{eco} for RCP2.6 by 2.6°C, and by 5.7 °C for RCP8.5 (Fig. 3c). On the other hand, boreal and arctic biomes will still remain within the safety margin, with T_{opt}^{eco} staying above $T_{max\,gs}^{air}$ except under the RCP8.5 high warming scenario (Fig. 3b and Supplementary Fig. 13).

Despite the lack of in situ observational evidence for GPP acclimation to the ongoing warming trend, we tested a simple future acclimation law based on the space-for-time substitution assumption that T_{opt}^{eco} will evolve proportionally to $T_{max\,gs}^{air}$, following on the spatial temperature

sensitivity of T_{opt}^{eco} to $T_{max\ gs}^{air}$ in Fig. 1d. We took the differences in precipitation levels into account, so that areas that become wetter also exhibit faster acclimation. Even with this assumed acclimation law, $T_{max\ gs}^{air}$ will still surpass T_{opt}^{eco} by 1.7 °C under RCP2.6 and by 2.5 °C under RCP8.5 for tropical evergreen forests (Fig. 3c). Not accounting for precipitation levels in the acclimation rates produced similar results (Supplementary Figs. 14 and 15).

Our global-scale analysis of T_{opt}^{eco} derived from globally distributed point measurements of eddy covariance and space-borne observations of proxies of vegetation productivity is a first attempt to diagnose the global distribution of ecosystem-scale temperature optima of photosynthesis. It should be noted, however, that hypotheses about that thermal acclimation of T_{opt}^{eco} are still highly uncertain, because ecosystem adjustments can lag substantially behind the rate of future warming, particularly for forests. The acclimation of plants to increasing atmospheric CO_2 concentration and to changes in other environmental factors (e.g. VPD) was also not considered in the current analyses. Constraining the spatially observed temperature sensitivity of T_{opt}^{eco} over time is a priority for future studies. Continuous monitoring and dedicated manipulative experiments could improve our understanding of the features of T_{opt}^{eco} and thermal acclimation in earth system models[34].

Methods

FLUXNET data The half-hourly eddy-covariance Gross Primary Productivity (GPP) data were obtained from FLUXNET datasets, and were quality-controlled, filtered against low turbulence, and gap-filled using consistent methods, as described by Papale et al.[35]. Only freely available FLUXNET data were used in this study. All the half-hourly GPP data were aggregated into daily

accumulated GPP for further estimates of the optimal temperature for vegetation productivity. We included only site-years with more than 80% of half-hourly data available. A total of 153 individual FLUXNET sites with 663 site-years of GPP data were used in this study.

Near-infrared reflectance of terrestrial vegetation Badgley et al.[17] have recently proposed a new approach for estimating vegetation photosynthetic capacity by remote sensing, i.e. the near-infrared reflectance (NIR) of terrestrial vegetation (NIR_V), which can differentiate between the confounding effects of background brightness, leaf area and the distribution of photosynthetic capacity with depth in canopies[17]. NIR_V is calculated as the product of total scene NIR reflectance (NIR_T) and Normalized Difference Vegetation Index (NDVI)[17]. As a proxy of photosynthesis, NIR_V is suggested to be strongly correlated with Solar-induced Chlorophyll Fluorescence (SIF), a direct index of photons intercepted by chlorophyll, and shows higher correlation with observed GPP than NDVI[17]. We used satellite-derived NIR_V to calculate and map the optimal air temperature for vegetation productivity at an ecosystem scale (T_{opt}^{eco}). Following Badgley et al.[17], we calculated 16-day NIR_V for 2001-2013 as the product of Moderate Resolution Imaging Spectroradiometer (MODIS) 16-day NIR reflectance and MODIS 16-day NDVI, both of which were derived from the MOD13A2 Vegetation Index Product with a spatial revolution of 1 km. Only positive NIR_V values were used in the analysis. Pixels with a mean annual NDVI>0.1 were defined as the vegetated area.

Normalized Difference Vegetation Index The Normalized Difference Vegetation Index (NDVI) is a vegetation index defined as the ratio of the difference between NIR and red visible reflectance to their sum, and is widely used to represent vegetation greenness[36]. To account for uncertainties from different satellite datasets, three independent NDVI datasets were utilized,

253 including Global Inventory Modeling and Mapping Studies (GIMMS) Advanced Very High
254 Resolution Radiometer (AVHRR) biweekly NDVI, Terra Moderate Resolution Imaging
255 Spectroradiometer (MODIS) 16-day NDVI and Satellite Pour l'Observation de la Terre
256 Vegetation (SPOT Vegetation) 10-day NDVI. The three NDVI datasets spanned the last three
257 decades: 1982-2009 for AVHRR NDVI datasets, 2000-2009 for MODIS NDVI datasets, and
258 1999-2009 for SPOT NDVI datasets, with the spatial resolutions of 8 km, 1 km, and 1 km,
259 respectively. All NDVI datasets have been corrected to reduce the effects of volcanic aerosols,
260 solar angle, and sensor errors[18,37,38]. Pixels with a mean annual NDVI>0.1 were defined as the
261 vegetated area for each dataset.
262
263 **Enhanced Vegetation Index** The Enhanced Vegetation Index (EVI) is another vegetation index
264 designed to enhance the vegetation signal by minimizing canopy-soil variations and to improve
265 sensitivity over dense vegetation conditions[19], and is found to correlate well with estimated GPP
266 on a site-by-site basis[39]. We used a 16-day EVI dataset for the period of 2000-2009 with a spatial
267 resolution of 1 km from the MOD12A1 Vegetation Index Product. Effects from aerosols, solar
268 angle and sensor error have all been corrected[19].
269
270 **Sun-induced Chlorophyll Fluorescence** Chlorophylls in plant would absorb shortwave radiation
271 and dissipate the excess energy as light or heat. The longwave radiation re-emitted by
272 chlorophylls is referred as chlorophyll fluorescence. Recent studies have reported that remotely
273 sensed Sun-induced Chlorophyll Fluorescence (SIF) could serve as an indicator of photosynthesis
274 rate and it is well correlated with model-simulated GPP[40]. Following the previous studies[40,41], we
275 retrieved SIF from two different retrieval windows, 757 nm and 771 nm, as well as the two
276 polarization states, S and P using observation of Fourier Transform Spectrometer (FTS) on the

277 Japanese Greenhouse gases Observing SATellite (GOSAT)[20]. These diverse SIF samples of were
278 then aggregated into monthly gridded data at a spatial resolution of 2^o from June 2009 to June
279 2012.
280
281 **Vegetation distribution** We used MODIS land cover with the classification scheme of the
282 International Geosphere-Biosphere Programme (IGBP). The MODIS IGBP land cover data were
283 derived from the MOD12Q1 Land Cover Science Data Product at a spatial resolution of 1 km and
284 an updated digital Köppen-Geiger world map of climatic classification[42]. Within the vegetated
285 area defined by NDVI thresholds, the 17 land cover types were reclassified into 9 vegetation
286 types, namely evergreen needle-leaved forest (ENF), evergreen broad-leaved forest (EBF),
287 deciduous needle-leaved forest (DNF), deciduous broad-leaved forest (DBF), mixed forest (MF),
288 savannas, cropland, grassland and shrubland. Based on the main climates in the world Map of the
289 Köppen-Geiger climatic classification[42], grassland was further subdivided into temperate
290 grasslands, boreal and arctic tundra, and shrubland was further subdivided into temperate and
291 boreal shrubland. The grassland over the Tibetan Plateau was considered separately.
292
293 **Climate dataset** The gridded air temperature and precipitation data for the period of 1982-2013
294 were obtained from the CRU/NCEP 6-hourly dataset with a spatial resolution of 0.5^o. It should be
295 noted that near-surface air temperature (the thermodynamic temperature of the air at a height of 2
296 m) rather than land surface temperature (the temperature of underlying canopy surface) were used
297 to calculate T_{opt}^{eco} considering the fact that for tropical regions, especially tropical forests, daytime
298 surface temperature can be much lower than daytime air temperature as a result of the
299 evapotranspiration effects[43]. Furthermore, the climate forcing data of global ecosystem models
300 are generally air temperature instead of surface temperature (e.g. ref 44, 45). Corresponding to

the temporal resolutions of MODIS, AVHRR and SPOT datasets, respectively, the 6-hourly climate data were aggregated into 16-day, biweekly, and 10-day values before further analyses. Given the different spatial resolutions of satellite observations and climate data, we simply extracted time series of daily maximum air temperature and precipitation from the aggregated CRU/NCEP data for each pixel of the sets of remotely sensed data. The daily maximum air temperature (T_{max}^{air}) of the growing season averaged over 2001-2013 was calculated as the current mean growing-season daily maximum air temperature ($T_{max\ gs}^{air}$). Information on the growing season was derived from the study by Zhu et al.[46], which was first determined from the GIMMS Leaf Area Index data set (GIMMS LAI_{3g}) using a Savitzky-Golay filter and then refined by excluding the ground-freeze period identified by the Freeze/Thaw Earth System Data Record (see details in ref 46). We also documented the temperature thresholds at which the growing season begins and ends for each year. Temperature thresholds were averaged over 2001-2013 for the onset and end of the growing season, respectively. We also used WATCH Forcing Data Methodology to ERA-Interim data with a temporal resolution of three hours (WFDEI)[47].

We also used climate projections for the end of the 21st century (2091-2100) under the RCP2.6, RCP4.5 and RCP.85 scenarios[32] to determine the impact of future warming on vegetation productivity. Considering the mismatch between CRU/NCEP datasets and outputs from General Circulation Models (GCM) for current climate conditions, we generated future temperature and precipitation data by adding the relative changes in GCM-derived climate projections to the current climate. $T_{max\ gs}^{air}$ for the late 21st century was estimated using the same temperature thresholds as for the current $T_{max\ gs}^{air}$. All GCM projections were resampled to a resolution of 1^{o} using first-order conservative interpolation method[48].

Analysis We estimated local T_{opt}^{eco} by examining the temperature response curve of MODIS NIR_V. Following Yuan et al.[27] and Niu et al.[49], NIR_V time series throughout the entire monitoring period and the corresponding temperature data were grouped into 1^oC-temperature bins for each pixel within vegetated areas. We used the 90% quantile of the NIR_V data as the response of NIR_V within each temperature bin due to the potential influences of other environmental constraints like clouds and droughts. We next calculated the running means of every three temperature bins to develop the temperature response curve of NIR_V. The T_{opt}^{eco} was then determined from the response curve at which NIR_V was maximized (Supplementary Fig. 16). Note that T_{opt}^{eco} may not be detected for some pixels where the maximum NIR_V was only attained at either end of the response curve. The derivation of T_{opt}^{eco} is robust to the choice of a particular climate-forcing dataset (Supplementary Fig. 2). Instead of using the temperature corresponding to the maximum 90^{th} quantile NIR_V to calculate T_{opt}^{eco}, we also applied nonlinear regression of the photosynthetic temperature response data (Eq.1) to estimate T_{opt}^{eco}, which produced similar results (Supplementary Fig. 2):

$$NIR_{V(T)} = NIR_{V(OPT)} - b(T - T_{opt}^{eco})^2 \quad \text{(Eq.1)}$$

where $NIR_{V(T)}$ is the NIR_V value at a daily maximum temperature T, b is a parameter describing the spread of the parabola[33,50]. T_{opt}^{eco} is the vertex of each fit and $NIR_{V(OPT)}$ is the NIR_V value at T_{opt}^{eco}. Finally, we used daily mean air temperature (T_{mean}^{air}) instead of T_{max}^{air} to calculate T_{opt}^{eco}. In this test, T_{opt}^{eco} derived from T_{mean}^{air} is smaller than T_{opt}^{eco} estimated from T_{max}^{air}, but the two variables were strongly spatially correlated (Supplementary Fig. 6).

We investigated the relationship between T_{opt}^{eco} and climate variables by averaging T_{opt}^{eco} in the climate space with 1-°C intervals of mean annual T_{max}^{air} averaged over the growing season ($T_{max\,gs}^{air}$) and 100-mm intervals of mean annual precipitation (MAP) (Fig. 1d). For each MAP interval, we calculated the 'apparent' spatial sensitivity of T_{opt}^{eco} in response to changes in $T_{max\,gs}^{air}$ using bootstrapping method. We performed the linear regression analysis 1000 times by randomly selecting a subset of 80% of the samples from pairs of T_{opt}^{eco} and $T_{max\,gs}^{air}$ within each MAP interval. The mean and SD of the 1000 temperature sensitivity of T_{opt}^{eco} were subsequently estimated along the MAP gradient.

Air temperature, atmospheric vapor pressure deficit (VPD) and solar radiation usually co-vary in time and space, so that the empirical observation of spatial patterns of T_{opt}^{eco} in this study cannot be unambiguously attributed to air temperature as a single explaining factor of T_{opt}^{eco}. Under conditions of high temperature, atmospheric VPD increases, soil moisture decreases with a lag, stomatal conductance, xylem conductance and hence carbon assimilation rates (GPP at the ecosystem-scale) decrease to prevent exceedingly low leaf water potentials and resulting plant tissue damage from cavitation[51]. We show that across climatic gradients T_{opt}^{eco} is systematically higher at high maximum air temperatures but not systematically lower at high VPD conditions (Supplementary Fig. 17). To examine whether VPD can substantially affect the relationship between T_{opt}^{eco} and $T_{max\,gs}^{air}$, we further calculated the partial ('intrinsic') sensitivity of T_{opt}^{eco} to $T_{max\,gs}^{air}$ in each grid point based on the following bilinear regression:

$$T_{opt}^{eco} = k_0 + k_1 \times T_{max\,gs}^{air} + k_2 \times VPD + k_3 \times VPD \times T_{max\,gs}^{air} \quad \text{(Eq.2)}$$

where the partial sensitivity of T_{opt}^{eco} to $T_{max\,gs}^{air}$ is defined as k_1 in Eq. 2 under each VPD bin. Then we compared the partial sensitivity with the apparent sensitivity of T_{opt}^{eco} to $T_{max\,gs}^{air}$ estimated using abovementioned linear regression between T_{opt}^{eco} and $T_{max\,gs}^{air}$ for each VPD bin. As shown in Supplementary Fig. 18, although the apparent sensitivity of T_{opt}^{eco} to $T_{max\,gs}^{air}$ is generally lower than the partial ('intrinsic') sensitivity of T_{opt}^{eco} to $T_{max\,gs}^{air}$ the apparent sensitivity to $T_{max\,gs}^{air}$ remains positive even when VPD is taken into account excepted under very high VPD bins (higher than ~4.5 kPa) representing less than 1% of the study area. These results suggest that the patterns of T_{opt}^{eco} are not dominated by high VPD reducing photosynthesis, as an indirect effect of higher air temperature increasing VPD. Moreover, we also calculated the percentiles of downward shortwave solar radiation (Rad) at the time of year when T_{opt}^{eco} is observed for the 16-day averaged Rad distribution. As shown in Supplementary Fig. 19, the Rad value when T_{opt}^{eco} was retrieved from global observations were below the 95th percentile in the 16-day Rad distribution for ~80% of the study area, which is mainly in mid and low latitudes such as Africa, India, Australia, eastern Brazil and southern and southwestern of North America. By comparison, for most part of boreal regions, part of south China, southeastern US, as well as part of South America, the timing of T_{opt}^{eco} is consistent the time of maximum solar radiation. This is because T_{opt}^{eco} in these regions generally appears in summer, which is also the period when solar radiation displays its maximum during the year.

The NIR_V-derived T_{opt}^{eco} was compared with T_{opt}^{eco} estimated using GPP data from 153 eddy covariance sites. For each site, we extracted and averaged T_{opt}^{eco} values within a 3×3 pixel window around the site from the NIR_V-derived T_{opt}^{eco} map, and calculated the SD of the nine T_{opt}^{eco} values

within the window. T_{opt}^{eco} was determined for each site-year with daily-accumulated GPP and corresponding temperature data from flux tower observations, applying the same method to estimate local T_{opt}^{eco} using NIR_V datasets. A robust estimate of T_{opt}^{eco} can be derived for 125 sites (Supplementary Table 1). For each site, we calculated the mean and SD of T_{opt}^{eco} across different years. The results show that NIR_V-derived T_{opt}^{eco} is comparable with that estimated independently from measurements of flux-tower eddy covariance (Fig. 1b).

We compared the spatial distribution of T_{opt}^{eco} derived from NIR_V with the one obtained from NDVI datasets. Consistent spatial patterns of T_{opt}^{eco} are derived from each of the three NDVI datasets (Supplementary Fig. 20). A global composite map of T_{opt}^{eco} (Supplementary Fig. 3) was then generated by averaging over estimates derived from the three NDVI datasets. Given the inconsistent spatial resolutions of the different products, we resampled T_{opt}^{eco} to a common grid of 8 km before averaging. T_{opt}^{eco} from NDVI datasets generally show a spatial pattern similar to that from NIR_V, but with smaller NDVI-derived T_{opt}^{eco} values for central Australia and southern South America (Supplementary Fig. 3). We compared the spatial distribution of T_{opt}^{eco} derived from NIR_V with that from MODIS EVI data during 2001-2013, and found that the EVI derived T_{opt}^{eco} shows very similar spatial pattern to that of NIR_V derived T_{opt}^{eco} (Supplementary Fig. 4). The distribution of T_{opt}^{eco} derived from NIR_V and from GOSAT SIF datasets also have similar spatial patterns, even though the NIR_V-derived T_{opt}^{eco} is higher in tropical regions, particularly in cultivated areas of southeastern Brazil (Supplementary Fig. 5).

The NIR_V-derived T_{opt}^{eco} was compared with leaf-scale optimal temperature of maximum Rubisco-limited carboxylation rates (V_{cmax}) (T_{opt}^{leaf}) from leaf-scale measurements[5]. The compilation of data from Kattge and Knorr[5] contains 48 available measurements of T_{opt}^{leaf} values for 36 species. For T_{opt}^{leaf} measurements with site location (longitude and latitude) reported, we extracted and averaged T_{opt}^{eco} values within a 3×3 pixel window around the site from the NIR_V-derived T_{opt}^{eco} map. For T_{opt}^{leaf} measurements without the information of site location, we calculated the average NIR_V-derived T_{opt}^{eco} values across pixels with both the same growing season mean temperature and the same plant functional type as the corresponding site. As shown in Supplementary Fig. 7, T_{opt}^{eco} is generally lower than T_{opt}^{leaf}.

To account for potential changes in T_{opt}^{eco} under future warming, we estimated the acclimated T_{opt}^{eco} for vegetation productivity by the end of the 21st century (2091-2100), using recent IPCC climate projections[32]. Given the relatively large uncertainties of precipitation projections, we considered two future precipitation scenarios. For the first scenario, we estimated acclimated T_{opt}^{eco} pixel by pixel using the temperature sensitivity of T_{opt}^{eco} under the present MAP level, assuming that MAP does not change between the end of the 21st century. For the second scenario, we accounted for in MAP, and the acclimated T_{opt}^{eco} was calculated pixel by pixel using the temperature sensitivity of T_{opt}^{eco} under the projected MAP level for 2091-2100. Acclimated T_{opt}^{eco} was averaged across the GCMs under each scenario.

Data Availability

All data is available in the main text or the supplementary information. All computer codes used in this study can be provided by the corresponding author upon reasonable requests.

References

1. Berry, J. & Bjorkman, O. Photosynthetic response and adaptation to temperature in higher plants. *Annual Review of Plant Physiology* **31**, 491-543 (1980).
2. Hughes, L. Biological consequences of global warming: is the signal already apparent? *Trends in Ecology & Evolution* **15**, 56-61 (2000).
3. Niu, S. *et al.* Climatic warming changes plant photosynthesis and its temperature dependence in a temperate steppe of northern China. *Environmental and Experimental Botany* **63**, 91-101 (2008).
4. Way, D. A., Yamori, W. Thermal acclimation of photosynthesis: on the importance of adjusting our definitions and accounting for thermal acclimation of respiration. *Photosynthesis research* **119**, 89-100 (2014).
5. Kattge, J., Knorr, W. Temperature acclimation in a biochemical model of photosynthesis: a reanalysis of data from 36 species. *Plant, cell & environment* **30**, 1176-1190 (2007).
6. Lloyd, J., Farquhar, G. D. Effects of rising temperatures and [CO_2] on the physiology of tropical forest trees. *Philosophical Transactions of the Royal Society B: Biological Sciences* **363**, 1811-1817 (2008).
7. Sage, R. F., Kubien, D. S. The temperature response of C_3 and C_4 photosynthesis. *Plant, Cell & Environment* **30**, 1086-1106 (2007).
8. Field, C. B., Randerson, J. T., Malmström, C. M. Global net primary production: combining ecology and remote sensing. *Remote sensing of Environment* **51**, 74-88 (1995).

9. Niinemets, Ü. Global-scale climatic controls of leaf dry mass per area, density, and thickness in trees and shrubs. *Ecology* **82**, 453-469 (2001).

10. Williams, A. P. *et al.* Temperature as a potent driver of regional forest drought stress and tree mortality. *Nature Climate Change* **3**, 292-297 (2013).

11. Yin, X., Struik, P. C_3 and C_4 photosynthesis models: an overview from the perspective of crop modelling. *NJAS-Wageningen Journal of Life Sciences* **57**, 27-38 (2009).

12. N. G. Smith, S. L. Malyshev, E. Shevliakova, J. Kattge, J. S. Dukes, Foliar temperature acclimation reduces simulated carbon sensitivity to climate. *Nature Climate Change* **6**, 407 (2016).

13. Mercado, L. M. *et al.* Large sensitivity in land carbon storage due to geographical and temporal variation in the thermal response of photosynthetic capacity. *New Phytologist* **218**, 1462-1477 (2018).

14. Corlett, R. T. Impacts of warming on tropical lowland rainforests. *Trends in Ecology & Evolution* **26**, 606-613 (2011).

15. Doughty, C. E., Goulden, M. L. Are tropical forests near a high temperature threshold? *Journal of Geophysical Research: Biogeosciences* **113**, G00B07 (2008).

16. Baldocchi, D., Falge, E., Gu, L. *et al.* FLUXNET: A new tool to study the temporal and spatial variability of ecosystem-scale carbon dioxide, water vapor, and energy flux densities. *Bulletin of the American Meteorological Society* **82**, 2415-2434 (2001).

17. Badgley, G., Field, C. B., Berry, J. A. Canopy near-infrared reflectance and terrestrial photosynthesis. *Science Advances* **3**, e1602244 (2017).

18. Pinzon, J. E., Tucker, C. J. A non-stationary 1981-2012 AVHRR $NDVI_{3g}$ time series. *Remote Sensing* **6**, 6929-6960 (2014).

19. Huete, A. *et al.* Overview of the radiometric and biophysical performance of the MODIS vegetation indices. *Remote Sensing of Environment* **83**, 195-213 (2002).

20. Joiner, J., Yoshida, Y., Vasilkov, A., Middleton, E. First observations of global and seasonal terrestrial chlorophyll fluorescence from space. *Biogeosciences* **8**, 637-651 (2011).

21. Ma, S., Osuna, J. L., Verfaillie, J. *et al.* Photosynthetic responses to temperature across leaf-canopy-ecosystem scales: a 15-year study in a Californian oak-grass savanna. *Photosynthesis research* **132**, 277-291 (2017).

22. Catovsky, S., Holbrook, N., Bazzaz, F. Coupling whole-tree transpiration and canopy photosynthesis in coniferous and broad-leaved tree species. *Canadian Journal of Forest Research* **32**, 295-309 (2002).

23. Doughty, C. E., Goulden, M. L. Seasonal patterns of tropical forest leaf area index and CO_2 exchange. *Journal of Geophysical Research: Biogeosciences* **113**, G00B06, doi:10.1029/2007JG000590 (2008).

24. Wu, J. *et al.* Partitioning controls on Amazon forest photosynthesis between environmental and biotic factors at hourly to interannual timescales. *Global Change Biology*, **23**, 1240-1257 (2017).

25. Gunderson, C. A., O'Hara, K. H., Campion, C. M., Walker, A. V., Edwards, N. T. Thermal plasticity of photosynthesis: the role of acclimation in forest responses to a warming climate. *Global Change Biology* **16**, 2272-2286 (2010).

26. Mooney, H. A., Björkman, O., Collatz, G. J. Photosynthetic acclimation to temperature in the desert shrub, Larrea divaricata I. Carbon dioxide exchange characteristics of intact leaves. *Plant Physiology* **61**, 406-410 (1978).

27. Yuan, W. *et al.* Thermal adaptation of net ecosystem exchange. *Biogeosciences* **8**, 1453-1463 (2011).

28. Doughty, C. E. An in situ leaf and branch warming experiment in the Amazon. *Biotropica* **43**, 658-665 (2011).

29. Koch, G. W., Amthor, J. S., Goulden, M. L. Diurnal patterns of leaf photosynthesis, conductance and water potential at the top of a lowland rain forest canopy in Cameroon: measurements from the Radeau des Cimes. *Tree Physiology* **14**, 347-360 (1994).

30. Tribuzy, E. S. *Variações da temperatura foliar do dossel eo seu efeito na taxa assimilatória de CO_2 na Amazônia Central*, Universidade de São Paulo (2005).

31. White, A., Cannell, M. G., Friend, A. D. CO_2 stabilization, climate change and the terrestrial carbon sink. *Global Change Biology* **6**, 817-833 (2000).

32. IPCC, *Climate Change 2013: The Physical Science Basis. Contribution of Working Group I to the Fifth Assessment Report of the Intergovernmental Panel on Climate Change*. (Cambridge University Press, Cambridge, UK, 2013).

33. Sendall, K. M. *et al.* Acclimation of photosynthetic temperature optima of temperate and boreal tree species in response to experimental forest warming. *Global Change Biology* **21**, 1342-1357 (2015).

34. Cavaleri, M. A., Reed, S. C., Smith, W. K., Wood, T. E. Urgent need for warming experiments in tropical forests. *Global Change Biology* **21**, 2111–2121 (2015).

35. Papale, D. *et al.* Towards a standardized processing of Net Ecosystem Exchange measured with eddy covariance technique: algorithms and uncertainty estimation. *Biogeosciences* **3**, 571-583 (2006).

36. Myneni, R. B., Ramakrishna, R., Nemani, R., Running, S. W. Estimation of global leaf area index and absorbed PAR using radiative transfer models. *IEEE Transactions on Geoscience and remote sensing* **35**, 1380-1393 (1997).

37. Maisongrande, P., Duchemin, B., Dedieu, G. VEGETATION/SPOT: an operational mission for the Earth monitoring; presentation of new standard products. *International Journal of Remote Sensing* **25**, 9-14 (2004).

38. Vermote, E. F., El Saleous, N. Z., Justice, C. O. Atmospheric correction of MODIS data in the visible to middle infrared: first results. *Remote Sensing of Environment* **83**, 97-111 (2002).

39. Rahman, A. F., Sims, D. A., Cordova, V. D., El-Masri, B. Z. Potential of MODIS EVI and surface temperature for directly estimating per-pixel ecosystem C fluxes. *Geophysical Research Letters* **32**, 156-171 (2005).

40. Frankenberg, C. *et al.* New global observations of the terrestrial carbon cycle from GOSAT: Patterns of plant fluorescence with gross primary productivity. *Geophysical Research Letters* **38**, 351-365 (2011).

41. Lee, J. E. *et al.* Forest productivity and water stress in Amazonia: observations from GOSAT chlorophyll fluorescence. *Proceedings of the Royal Society B Biological Sciences* **280**, 176-188 (2013).

42. Kottek, M., Grieser, J., Beck, C., Rudolf, B., Rubel, F. World map of the Köppen-Geiger climate classification updated. *Meteorologische Zeitschrift* **15**, 259-263 (2006).

43. Lian, X. *et al.* Spatiotemporal variations in the difference between satellite-observed daily maximum land surface temperature and station-based daily maximum near-surface air temperature. *Journal of Geophysical Research: Atmospheres* **122**, 2254-2268 (2017).

44. Krinner, G. *et al.* A dynamic global vegetation model for studies of the coupled atmosphere-biosphere system. *Global Biogeochemical Cycles* **19**, GB1015 (2005).

45. Oleson, K. *et al.* Technical description of version 4.5 of the Community Land Model (CLM). (2013).

46. Zhu, Z. *et al.* Greening of the Earth and its drivers. *Nature Climate Change*, **6**, 701-795 (2016).

47. Weedon, G. P. *et al.* The WFDEI meteorological forcing data set: WATCH Forcing Data methodology applied to ERA-Interim reanalysis data. *Water Resources Research* **50**, 7505-7514 (2014).

48. Jones, P. W., First-and second-order conservative remapping schemes for grids in spherical coordinates. *Monthly Weather Review* **127**, 2204-2210 (1999).

49. Niu, S. *et al.* Thermal optimality of net ecosystem exchange of carbon dioxide and underlying mechanisms. *New Phytologist* **194**, 775-783 (2012).

50. Battaglia, M., Beadle, C., Loughhead, S. Photosynthetic temperature responses of Eucalyptus globulus and Eucalyptus nitens. *Tree Physiology* **16**, 81-89 (1996).

51. Stocker, B. D. *et al.* Quantifying soil moisture impacts on light use efficiency across biomes. *New Phytologist* **218**, 1430-1449 (2018).

Acknowledgments: This work used eddy covariance data acquired by the FLUXNET community and in particular by the following networks: AmeriFlux (U.S. Department of Energy, Biological and Environmental Research, Terrestrial Carbon Program (DE-FG02-04ER63917 and DE-FG02-04ER63911)), AfriFlux, AsiaFlux, CarboAfrica, CarboEuropeIP, CarboItaly, CarboMont, ChinaFlux, Fluxnet-Canada (supported by CFCAS, NSERC, BIOCAP, Environment Canada, and NRCan), GreenGrass, KoFlux, LBA, NECC, OzFlux, TCOS-Siberia, USCCC. This

study was supported by the National Natural Science Foundation of China (41530528), the National Key R&D Program of China (2017YFA0604702). We acknowledge the financial support to the eddy covariance data harmonization provided by CarboEuropeIP, FAO-GTOS-CO, iLEAPS, Max Planck Institute for Biogeochemistry, National Science Foundation, University of Tuscia, Université Laval and Environment Canada and US Department of Energy and the database development and technical support from Berkeley Water Center, Lawrence Berkeley National Laboratory, Microsoft Research eScience, Oak Ridge National Laboratory, University of California-Berkeley, University of Virginia. P.C., J.P., and I.A.J. would like to acknowledge the financial support from the European Research Council Synergy grant ERC-SyG-2013-610028 IMBALANCE-P. I.A.J. acknowledges the Methusalem funding of the Flemish Community through the Research Council of the University of Antwerp. T.F.K. was supported by the NASA Terrestrial Ecology Program IDS Award NNH17AE86I.

Author contributions: S.L.P. designed the research; M.T.H. performed the analysis; S.L.P. drafted the paper; and all authors contributed to the interpretation of the results and to the text.

Competing interests: Authors declare no competing interests.

Fig. 1 | Distribution of ecosystem-scale optimal temperature (T_{opt}^{eco}) for vegetation productivity derived from FLUXNET and satellite-based data for near-infrared reflectance of vegetation (NIR_V). a, Relationship between mean annual daily maximum air temperature during the growing season ($T_{max\,gs}^{air}$) and T_{opt}^{eco} derived from daily measurements of photosynthesis across FLUXNET eddy-covariance sites. The dotted gray line represents y=x. **b,** Relationship between T_{opt}^{eco} derived from FLUXNET data and T_{opt}^{eco} derived from NIR_V data. For each site, we extracted and averaged T_{opt}^{eco} values within a 3×3 pixel window around the site from NIR_V-derived T_{opt}^{eco} map, and calculated the SD of the nine T_{opt}^{eco} values within the window. The dotted gray line represents y=x. **c,** Spatial distribution of T_{opt}^{eco} for vegetation productivity (left panel), and T_{opt}^{eco} averaged by latitude (right panel). T_{opt}^{eco} is determined using NIR_V data calculated based on satellite observations from Moderate Resolution Imaging Spectroradiometer (MODIS). Areas of tropical forests based on current vegetation distribution are indicated by hatching. The circles on the map are colored according to the local value of T_{opt}^{eco} retrieved from GPP at the location of each FLUXNET site. The solid line and shaded area in the right panel indicate the mean and SD, respectively, of T_{opt}^{eco} summarized by latitude. **d,** T_{opt}^{eco} in the climate space (left panel) and the temperature sensitivity of T_{opt}^{eco} along the precipitation gradient (right panel). Each climate bin is defined by 1-^{o}C intervals of $T_{max\,gs}^{air}$ and 100-mm intervals of mean annual precipitation, based on current climate conditions averaged over 2001-2013. The solid line in the right panel represents the temperature sensitivity of T_{opt}^{eco} along the precipitation gradient, calculated as the slope of the linear regression between T_{opt}^{eco} and $T_{max\,gs}^{air}$ for a given precipitation level. The shaded area indicates the SD of temperature sensitivity of T_{opt}^{eco} estimated by bootstrapping.

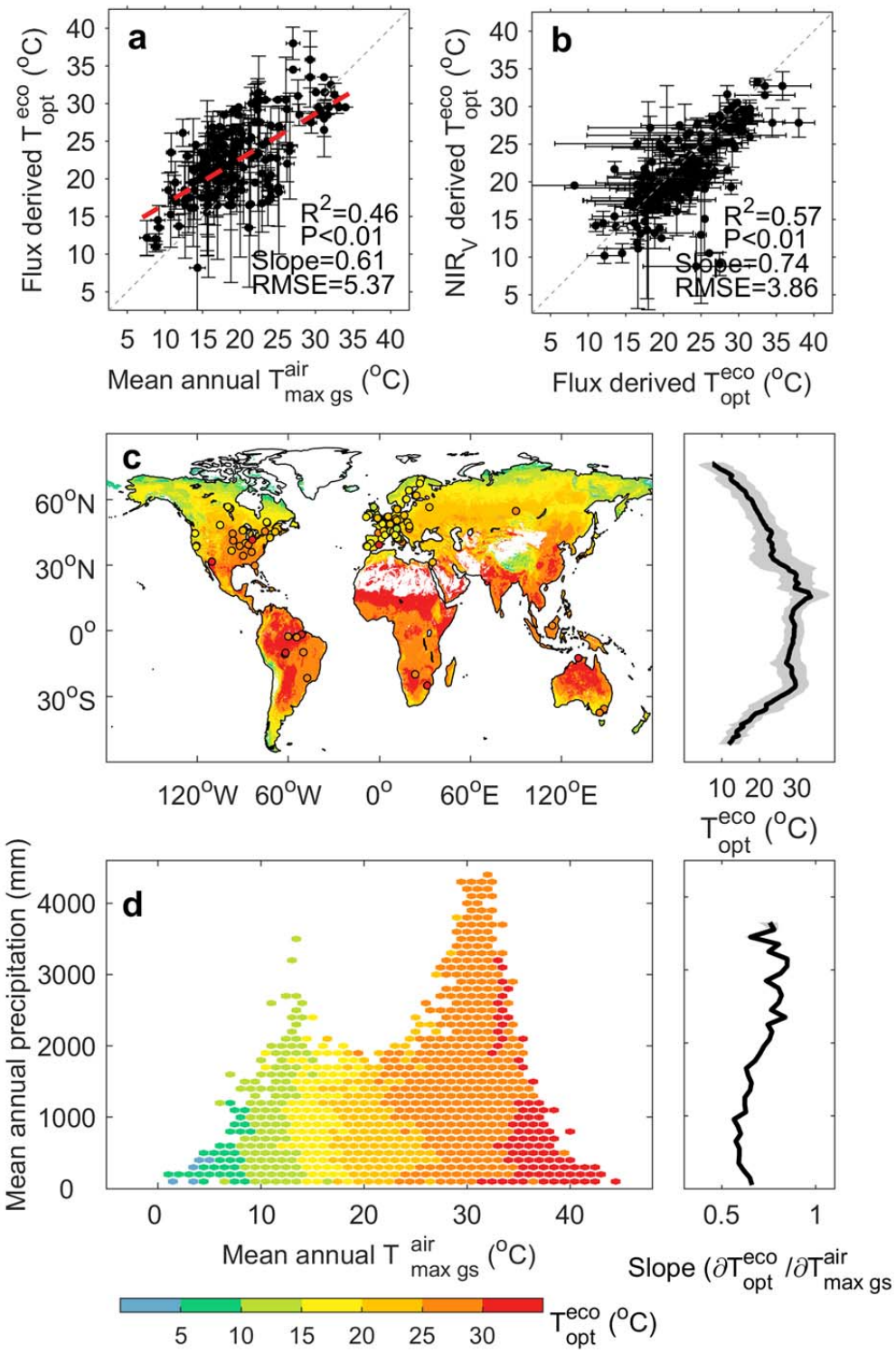
a
Flux derived T^{eco}_{opt} (^oC)
Mean annual $T^{air}_{max\ gs}$ (^oC)
R^2=0.46
P<0.01
Slope=0.61
RMSE=5.37
b
NIR_V derived T^{eco}_{opt} (^oC)
Flux derived T^{eco}_{opt} (^oC)
R^2=0.57
P<0.01
Slope=0.74
RMSE=3.86
c
60°N
30°N
0°
30°S
120°W 60°W 0° 60°E 120°E
10 20 30
T^{eco}_{opt} (^oC)
d
Mean annual precipitation (mm)
Mean annual $T^{air}_{max\ gs}$ (^oC)
Slope ($\partial T^{eco}_{opt} / \partial T^{air}_{max\ gs}$)
T^{eco}_{opt} (^oC)

611

612

Fig. 2 | Relationship between mean annual daily maximum air temperature during the growing season ($T^{air}_{max\ gs}$) and ecosystem-scale optimum temperature for vegetation productivity (T^{eco}_{opt}) across vegetation types. The error bars indicate the SDs of $T^{eco}_{opt}/T^{air}_{max\ gs}$ for each vegetation type: ENF, evergreen needle-leaved forest; EBF, evergreen broad-leaved forest; DNF, deciduous needle-leaved forest; DBF, deciduous broad-leaved forest; MF, mixed forest; Shrub, closed and open shrublands**.** The light-gray dotted line represents y=x. The dark-gray dotted line is y=0.76x+6.48 with the slope value shown in the bottom right. The red dotted line is the flux tower derived slope (0.61) from Fig. 1a.

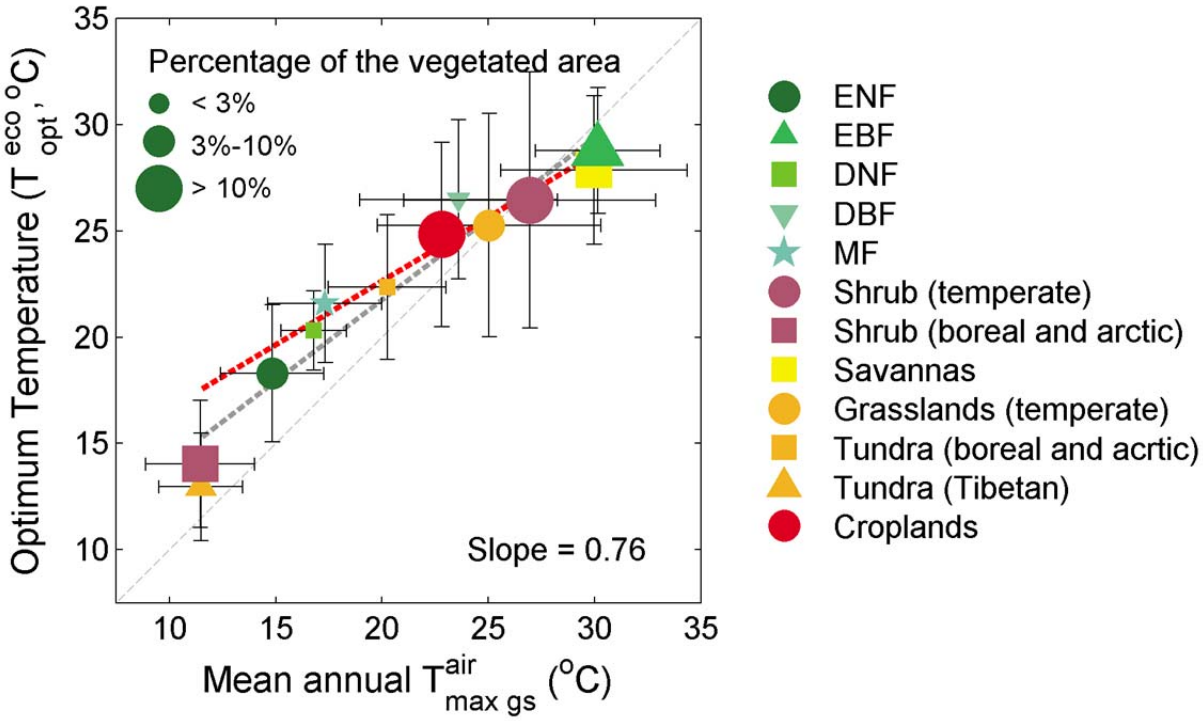

Fig. 3 | Change with latitude in ecosystem-scale optimal temperature for vegetation productivity (T_{opt}^{eco}) and daily maximum air temperature averaged over the growing season ($T_{max\,gs}^{air}$). a, Current T_{opt}^{eco} versus current $T_{max\,gs}^{air}$; **b,** Future T_{opt}^{eco} versus future $T_{max\,gs}^{air}$. Current T_{opt}^{eco} and $T_{max\,gs}^{air}$ are calculated using current temperature for 2001-2013, whereas acclimated T_{opt}^{eco} and future $T_{max\,gs}^{air}$ are calculated using temperature for 2091-2100 projected by General Circulation Models (GCMs) under the RCP4.5 scenario. Acclimated T_{opt}^{eco} is determined based on the projected temperature and temperature sensitivity of T_{opt}^{eco} using the annual precipitation level predicted for 2091-2100. The solid line and shaded area in each panel indicate the mean and SD, respectively, of T_{opt}^{eco} or $T_{max\,gs}^{air}$ summarized by latitude. **c,** Future T_{opt}^{eco} versus future $T_{max\,gs}^{air}$ for tropical evergreen forests. ** indicates that T_{opt}^{eco} is significantly lower than $T_{max\,gs}^{air}$ at P<0.01 in a paired t-test.